Multiscale spectral analysis of bathymetry on the flank of the Mid-Atlantic Ridge: Modification of the seafloor by mass wasting and sedimentation

John A. Goff

University of Texas Institute for Geophysics, Austin

Brian E. Tucholke

Woods Hole Oceanographic Institution, Woods Hole, Massachusetts

Abstract. The results of a multiscale spectral analysis of bathymetric data on the flank of the Mid-Atlantic Ridge are described. Data were collected during two cruises using Hydrosweep multibeam (tens of kilometers to ~0.2 km scale range) and Mesotech scanning pencil-beam sonar attached to remotely operated vehicle Jason (~1 km to ~0.5 m scale range). These data are augmented by visual data which enabled us to identify bathymetric profiles which are over unsedimented or thinly sedimented crust. Our analysis, therefore, is focused primarily on statistical characterization of basement morphology. Work is concentrated at two sites: site B on ~24 Ma crust in an outside-corner setting, and site D on ~3 Ma crust in an inside-corner setting. At site B we find that an anisotropic, band-limited fractal model (i.e., the "von Kármán" model proposed for abyssal hill morphology by *Goff and Jordan* [1988]) is not sufficient to describe the full range of scales observed in this study. Our observations differ from this model in two ways: (1) strike and cross-strike (dip) spectral properties converge for wavelengths smaller than ~300 m, and (2) in both strike and dip directions the fractal dimension changes at ~10 m wavelength, from ~1.27 at larger scales to ~1.0 at smaller scales. The convergence of strike and dip spectral properties appears to be associated with destruction of ridge-parallel fault scarps by mass wasting, which develops canyon-like incisions that cross scarps at high angles. The change in fractal dimension at ~10 m scale appears to be related to a minimum spacing of significant slope breaks associated with scarps which are created by faulting and mass wasting. At site D, although there is no significant abyssal hill anisotropy, the spectral properties at all scales are consistent with the von Kármán model. The fractal dimension at this site (~1.15) is less than at site B. This difference may be reflect different morphology related to crustal formation at inside-corner versus outside-corner position or, more likely, differences in the degree of mass wasting. The smoothing of seafloor morphology by sediments is evident in Hydrosweep periodograms where, relative to basement roughness, spectral power decreases progressively with decreasing wavelength.

Introduction

Abyssal hills are created at mid-ocean ridges by extrusive volcanism and faulting and modified through time by mass wasting and sedimentation; this simple fact is known, but the product of these four interacting processes is a complex, chaotic, multiscale morphology that defies simplistic (i.e., deterministic) quantitative description. We nevertheless are motivated to characterize abyssal hill morphology by quantitative means. It is in this way that we expect to make objective comparisons between different seafloor terrains subjected to different conditions, thereby to measure the influence of each process on the formation of abyssal hills, and ultimately to place hard constraints on physical models of these processes. Much of the effort in seafloor analysis in recent years therefore has concentrated on using statistical methods of quantification, which are suited to investigation of complex morphology. These include analysis of second-order statistical properties (i.e., the power or amplitude spectrum [e.g., *Neidell*, 1966; *Bell*, 1975; *Fox and Hayes*, 1985; *Gilbert and Malinverno*, 1988], covariance function [e.g., *Krause and Menard*, 1965; *McDonald and Katz*, 1969; *Yesyunin*, 1975; *Goff and Jordan*, 1988], and variogram [e.g., *Herzfeld et al.*, 1995]), fault statistics [e.g., *Edwards et al.*, 1991; *Carbotte and Macdonald*, 1994; *Cowie et al.*, 1994], seamount distributions [e.g., *Smith and Jordan*, 1988; *Smith and Cann*, 1993; *Bemis and Smith*, 1993], and spectral response to sediment loading [*Webb and Jordan*, 1993].

Central to all statistical methods of characterization is the assumption that there exists a multiplicity of scales. This is certainly true in abyssal hill terrain, where features exist from characteristic outer scales (from ~1 km up to a few tens of kilometers) down to basalt pillows, talus debris (~submeter scale), and smaller. We anticipate that understanding this full range of scales will be important. It is likely, for example, that faulting dominates the large-scale properties of abyssal hills (e.g., rms height and characteristic width and length) [e.g., *Lonsdale*, 1977; *Bicknell et al.*, 1987; *Goff et al.*, 1995] but that at smaller scales the importance of volcanic structures and mass wasting will in-

crease [*Lonsdale*, 1977; *Bicknell et al.*, 1987; *Smith and Cann*, 1993; *Tucholke et al.*, 1997a]. How might such a change in importance of processes be reflected in the statistics of scale? Numerical sedimentation models of *Webb and Jordan* [1993] suggest that the progressive effects of sedimentation are strongly scale-dependent; smaller-scale structures are subdued first, and as accumulation increases, larger- and larger-scale structures are blanketed. Can we support or contradict their predictions with multiscale statistical observation?

A common limitation in all observational studies relating to multiple scales is one of instrument resolution [e.g., *Cowie et al.*, 1994]: typically either the instrument is designed to cover a large region expeditiously and thus suffers from limited resolution, or the instrument is designed to investigate fine details of structure and cannot practically cover large areas. Two recent cruises to the Office of Naval Research's (ONR) Atlantic Natural Laboratory [*Tucholke et al.*, 1991] (Figure 1) were designed to address this problem by collecting multiscale bathymetric data within nested surveys, i.e., beginning with a large-scale survey conducted with wide-swath/low resolution instrumentation and continuing to progressively smaller surveys with progressively higher-resolution instruments. The survey instruments utilized in this study include the Hydrosweep swath-bathymetry system (aboard the R/V *Ewing*) and the Mesotech pencil-beam scanning profiler mounted on the deep-towed remotely operated vehicle (ROV) Jason operated by the Deep-Submergence Laboratory (DSL) of Woods Hole Oceanographic Institution. This combined data set provides coregistered bathymetric data which are valid over a continuous range of scales from ~100 km to ~0.5 m. Also acquired in the survey was intermediate-scale DSL-120 deep towed bathymetry, which proved unsuitable for statistical analysis but provided excellent base maps for geologic interpretation.

This paper presents the results of a spectral analysis of the multiscale bathymetric data to establish a statistical model of abyssalhill basement morphology which is valid over all scales of interest. This is the first attempt to conduct such a detailed quantitative analysis on mature abyssalhill morphology. Previous multiscale/multi-instrument statistical studies have focused either near the axis of mid-ocean ridges [*Goff and Kleinrock*, 1991; *Cowie et al.*, 1994] or on the continental rise [*Fox and Hayes*, 1985]. The results thus allow us for the first time to investigate quantitatively the effects of mass wasting and sedimentation in the abyssal hill environment. This study also has important implications for deep-water acoustic reverberation studies [e.g., *Robertsson et al.*, 1996], which are the focus of ONR's Acoustic Reverberation Special Research Program and from which this study derived its funding.

The analysis is concentrated on two areas where basement roughness is well developed and where sediment cover is minimal. The primary survey area is site B, about 300 km west of the Mid-Atlantic Ridge axis (Figure 1). Although this crust is relatively old (24 Ma), it has sediment cover that averages <30 m thick and lies mostly in ponds between abyssal hills. Fine-scale surveys at site B focused along an exposed, east facing fault scarp which video observations show to be virtually free of sediment cover. Site B represents our most comprehensive sampling of fine-scale morphology. Mesotech bathymetry profiles were obtained in both strike and cross-strike (dip) directions over the fault scarp (the strike direction is the orientation of abyssal hill lineaments).

The second site analyzed is site D (Figure 1), on ~3 Ma crust about 35 km off the ridge axis. Sediment cover here averages <6 m, and again the steeper slopes are essentially sediment-free. Thus at both of these sites the fine-scale roughness of mature,
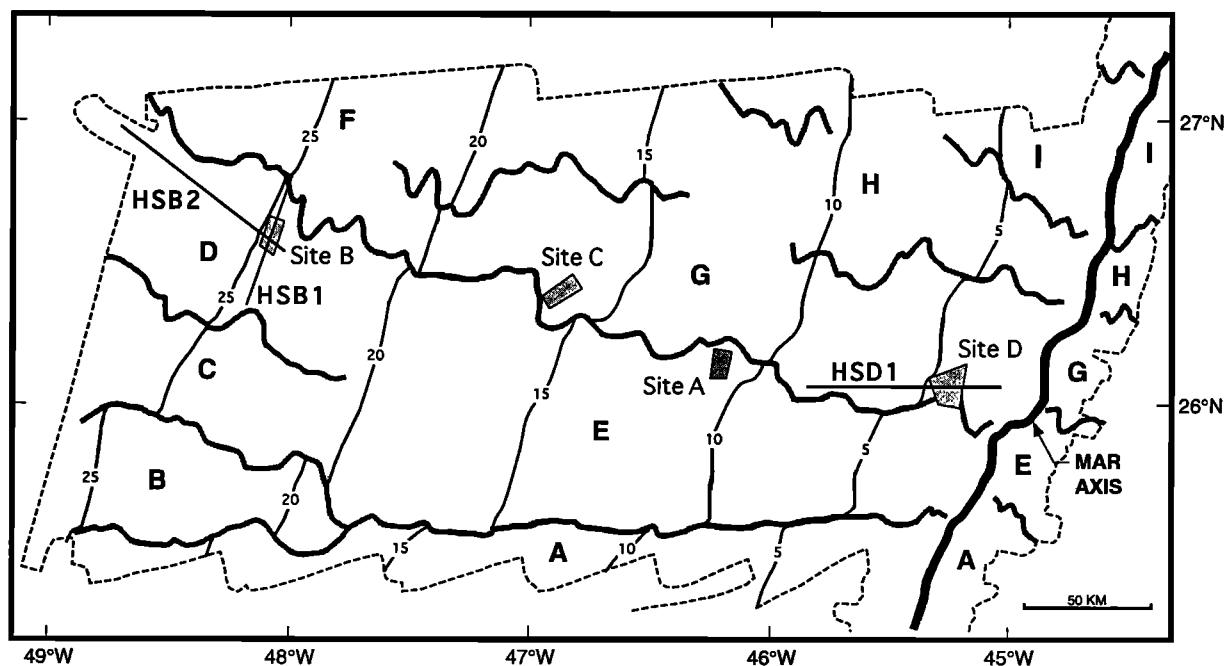

Figure 1. Area of the regional survey within the Office of Naval Research's Atlantic Natural Laboratory, including boundary of multibeam coverage (dashed lines), locations of four Deep Submergence Laboratory (DSL)-120 surveys (shaded regions, sites A-D), segment boundaries (thick lines), isochrons (thin lines labeled in m.y.), and the Mid-Atlantic Ridge (MAR) axis (thick solid line). Segments are identified by A-H, as shown. Profiles sampled from the gridded Hydrosweep data (HSB1, HSB2, and HSB3) used in this analysis are also shown. From *Tuchoke et al.* [1997a]. Modified with permission of the publisher, the Geological Society of America, Boulder, Colorado, USA. Copyright © 1997, The Geological Society of America, Inc. (GSA).

off-axis basement morphology can be explored without significant bias introduced by sediment cover. These two sites represent differences both in crustal age (3 Ma versus 24 Ma) and tectonic setting ("inside-corner" and "outside-corner" crust, as described below). We demonstrate that the larger-scale statistical character of basement and seafloor morphology differs significantly between these two sites.

In this paper the anisotropic von Kármán statistical model for abyssal hill morphology [*Goff and Jordan*, 1988] is tested. This model is essentially an upper-band-limited, simple fractal surface with different corner wavenumbers for the strike and dip directions (Figure 2). It is demonstrated in this paper that the von Kármán model is an oversimplified description, and a new conceptual model is provided based on our analysis.

Geological Setting of Survey Sites

The initial, regional survey of the Mid-Atlantic Ridge flank showed that the study area is divided into a series of coherent spreading segments which have accreted at the ridge axis over intervals ranging from ~10 m.y. to >28 m.y. [*Tucholke et al.*, 1997b] (Figure 1). Segment boundaries are marked by nontransform discontinuities which have had offsets of kilometers to a few tens of kilometers. With minor exceptions, isochron offsets in these discontinuities are right-stepping. The crust has been formed at a slow spreading rates (25-30 mm/yr) ridge axis, and abyssal hills consequently exhibit high rms roughness of 150-350 m [*Goff et al.*, 1995].

A distinctive characteristic of such slow spreading ridge segments is observed in differences between inside-corner (IC) crust, accreted at the ridge axis adjacent to the active non transform discontinuity, and outside-corner (OC) crust, accreted on the opposing side of the rift axis next to the inactive trace of the discontinuity [*Tucholke and Lin*, 1994]. Compared to OC crust, IC crust typically is elevated [*Severinghaus and Macdonald*, 1988]; its residual mantle Bouguer gravity anomalies are higher, implying thinner crust; volcanic features such as small seamounts are less frequently observed on thin IC crust; lower crustal gabbros and mantle peridotites are more frequently exposed; and faults are higher amplitude, more irregular and less linear in pattern. Recent analysis of the multibeam bathymetry in our survey area [*Goff et al.*, 1995] confirmed that there are strong IC/OC asym-
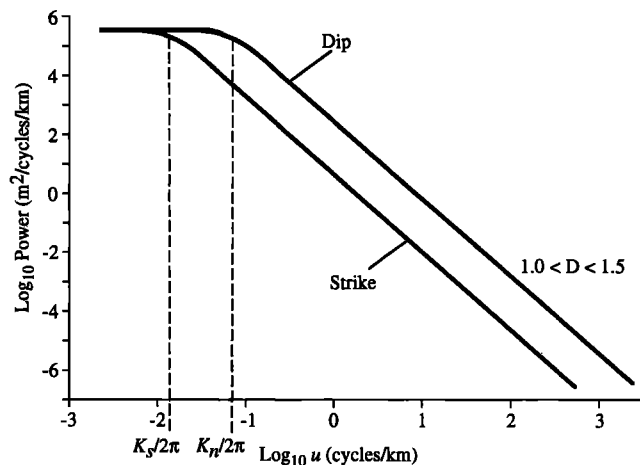

Figure 2. Schematic of the anisotropic von Kármán spectral model proposed by *Goff and Jordan* [1988] for abyssal hill morphology.

metries in the large-scale statistical characteristics of the fault-controlled abyssal hills. They found that IC abyssal hills had larger rms heights and characteristic widths than those at outside corners and the IC abyssal hills also were less lineated (i.e., they exhibit a lower anisotropic ratio, as defined by the ratio of corner wavenumbers in the dip and strike directions; see Figure 2).

These IC/OC differences have been attributed to low-angle detachment faulting near segment ends at the ridge axis [*Dick et al.*, 1981; *Karson*, 1990; *Tucholke and Lin*, 1994]. IC crust constitutes the footwall of the detachment fault, and as spreading occurs, much of the volcanic, upper crustal section is accreted and retained in the OC hanging wall. This process results in formation of OC crust with a relatively normal and complete crustal section similar to that at segment centers, but the IC footwall has thinned crust or even exposed mantle if the detachment fault is long-lived. Both IC and OC crust is cut by high-angle normal faults which form as the crust is uplifted into the rift mountains bounding the rift valley, but on inside corners these faults dissect the low-angle detachment surface [e.g., *Karson and Dick*, 1983]. The marked differences in fault patterns and abyssal hill development between IC and OC crust probably reflect differences in the amount of magmatic versus tectonic extension, in the brittle behavior of IC plutonic/ultramafic versus OC volcanic/diked oceanic crust, and in the pattern of near-field stresses around the adjacent nontransform discontinuity.

Fine-scale, near-bottom studies were conducted at four locations within the regional survey area, with two sites on IC crust and two on OC crust. All sites border the same right-stepping nontransform discontinuity between segments D-E and F-G (Figure 1). The isochron offset at the discontinuity adjacent to these sites ranges from 0.3 m.y. (5 km) to 1.5 m.y. (25 km). Two of the sites, site A (~10 Ma outside-corner crust) and site C (~17 Ma inside-corner crust), are not considered in the present analysis for reasons outlined in the following section. Site A is discussed in a separate paper which deals with faulting and mass wasting [*Tucholke et al.*, 1997a].

Site B, on 24 Ma crust, is in an outside-corner to near-segment-center setting. Regionally this crust exhibits long, linear abyssal hills (anisotropic ratio of ~3-5) which parallel seafloor isochrons. Within the DSL-120 survey (Plate 1) are three large, east facing fault scarps. The original fault plane(s) associated with these scarps have been extensively degraded by mass wasting [*Tucholke et al.*, 1997a]. Small canyon-like incisions, typically 100-200 m wide and at least tens of meters deep, cross the scarps at high angles. Some of the canyons cut more than 500 m into the footwalls behind the toes of the original fault scarps. Geomorphic trellis patterns appear in several areas along the scarps, wherein smaller gullies intersect the main canyons at nearly right angles (i.e., parallel to isochrons); the remaining skeleton of basaltic crust is a rectilinear pattern of sharply edged ridges. This morphology probably was caused by mass wasting along preexisting zones of weakness, e.g., fissures, joints, and small faults which parallel the spreading axis.

Video and still photography show that the intercanyon ridges are manganese-coated basalt which is free of sediment. The bases of the scarps typically are covered by gently dipping (~10°) talus ramps which are largely sediment covered and show only occasional basaltic cobbles and boulders breaking through the sediment drape.

In contrast to site B, site D is on young (~3 Ma) crust and is in an inside-corner setting (Figure 1 and Plate 2). Faulting at the IC edge of segment G is irregular and has an anisotropic ratio which

cannot reliably be distinguished from 1 (i.e., isotropic); however, toward the segment center immediately to the north, faults and abyssal hills are much more linear and are elongated parallel to seafloor isochrons. The site D survey centered on a fault-bounded valley, with unsedimented east facing and west facing scarps on the western and eastern margins of the valley, respectively (Plate 2). Unlike the scarps at site B, these scarps do not show pronounced incision due to mass wasting, although visual data suggest that small-scale mass wasting has significantly modified the original fault plane at scales of meters to tens of meters. Talus ramps are weakly developed at the bases of the scarps. Small pods of sediment-covered basaltic debris are observed, however, and they probably represent local slump masses. On the northwest side of the valley we surveyed a prominent bathymetric high exhibiting irregular fault patterns and blocky morphology (Plate 2). Visual data show that a large part of this crust is faulted pillow basalts, although there is at least one zone of massive, jointed, slab-sided blocks which appear to be gabbros. The volcanic upper crust in the site D survey area thus may be relatively thin or intermittent, as might be anticipated in this inside-corner setting.

Bathymetric Data

Instruments

The initial, regional survey aboard R/V *Ewing* obtained nearly 100% Hydrosweep bathymetric coverage over an area spanning three ridge segments along axis (~25°25'N to ~27°10'N) and crustal ages from 0 to ~28 Ma (~400 km) on the west flank of the Mid-Atlantic Ridge (Figure 1). These data were gridded at a 200 m interval, which is slightly larger than the typical echosounder beam footprint (in 4 km water depth the 2° beam footprint ranges from 140 m at nadir to 200 m at the outer beam). Hydrosweep profiles used in this paper were sampled from these gridded data.

Subsequent to the *Ewing* cruise, we conducted small-scale, near bottom surveys aboard R/V *Knorr*, focusing on four small sites (50-70 km^2) within the regional survey (Figure 1). Each site was first surveyed using the DSL-120 sonar system, which collected 120 kHz side-scan and split-beam swath bathymetry. Although an unfortunate accident during the first lowering damaged the DSL-120 electronics and rendered the bathymetric data unsuitable for statistical analysis, the data to be proved excellent for regional mapping and geologic interpretation.

Following DSL-120 surveys the ROV Jason was deployed to survey small regions (0.1-1.0 km^2) within sites A, B, and D, operating at altitudes of 0 to ~30 m. Jason carried a Mesotech pencil-beam scanning bathymetric sonar which operates at 675 kHz with a beam width of 1°. It produces a swath of bathymetric data by physically sweeping the transducer head back and forth across the Jason track. Data density is therefore highly nonuniform: in the along-track direction we obtain one sample per sweep (typically, ~3 m along-track, depending on vehicle speed), whereas in the cross-track direction ping rate and sweep speed determine the sampling density (generally less than 0.5 m). The maximum scale along-track is simply the length of the track (we use track lines ranging from ~280 m to ~1 km long), whereas the maximum scale cross-track is determined by the swath width (~20-50 m). Along-track profiles are generated by an algorithm which selects from each sweep one point closest to a chosen profile line. The intention of this procedure is to obtain as smooth and uniform a profile as possible from an otherwise irregular

sample space. Cross-track profiles are taken from a single sweep, which generally ranges between 50 and 100 sample points. Spectral analysis requires resampling of data at constant interval.

Data Profiles

Site B. Site B is our most comprehensive survey using the Mesotech system, with sampling in both strike and dip directions over a region largely sediment free. Typical sediment cover is shown in Figure 3. In Figure 3a a manganese-coated basaltic scarp dips eastward at ~45°. Sediments fill local lows in the irregular surface but do not appear to significantly alter the seafloor morphology at the resolution scale of the Mesotech instrument (~0.5 m). The scarp in Figure 3b also is manganese-coated basalt, dipping southward at ~70°-90°. The scarp itself is nearly devoid of sediments, but lightly sedimented talus is seen at the base of the scarp.

Locations of Mesotech profiles presented in this paper are shown in Plate 1, overlaid on the DSL-120 bathymetry. The "dip" profiles are not perpendicular to strike: line MB7 is oriented at ~60° to strike and line MB4 is ~45°; the survey design was not centered on statistical characterization, so we must use the track lines available. The "strike" profiles do parallel the strike of fault scarps and abyssal hills. All along-track Mesotech profiles suitable for analysis are presented (strike lines MB1 to MB3, and dip lines MB4 and MB7), but only a few of the thou-
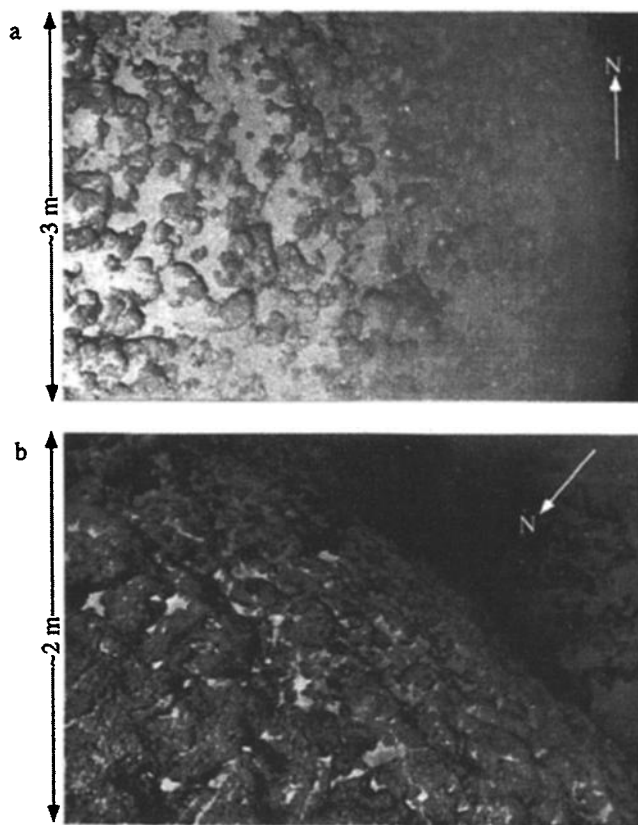
Figure 3. Electronic still-camera images from site B (locations in Plate 1b). (a) Scarp, dipping ~45° eastward, consisting of thinly sedimented, manganese-coated basalt. Scale is approximately 3 m top-to-bottom at left edge. (b) Scarp, dipping ~70°-90° to the south, consisting of manganese-coated basalt and thinly sedimented talus at base. Scale is approximately 2 m top-to-bottom at left edge.
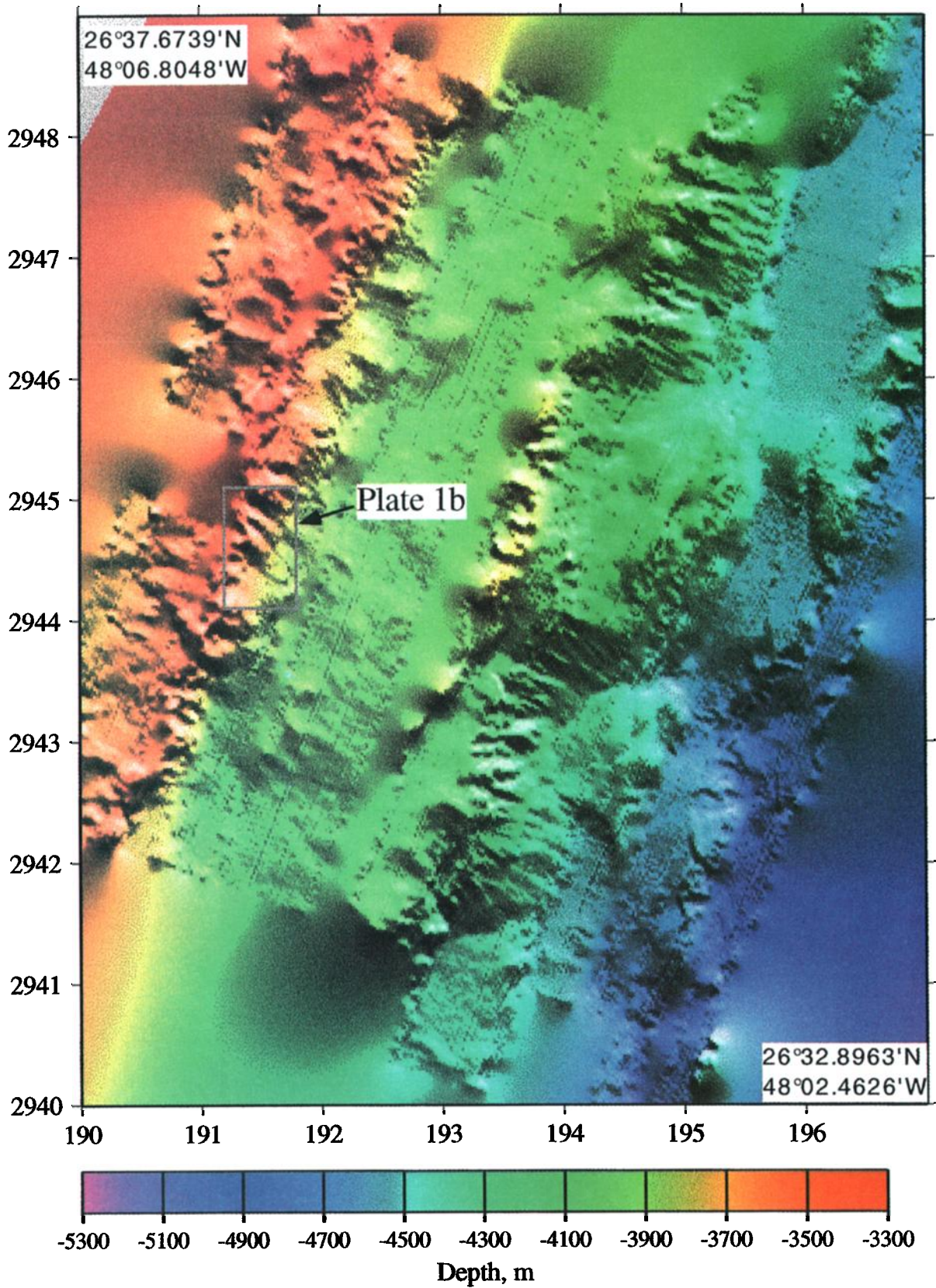
Plate 1a. Color contoured, shaded relief image of gridded DSL-120 bathymetry at site B (see Figure 1). Box coordinates are in Universal Trans-Mercator units (km), and latitude and longitude of the upper left and lower right corners of the box are given. Artificial Sun illumination is from N20°E.
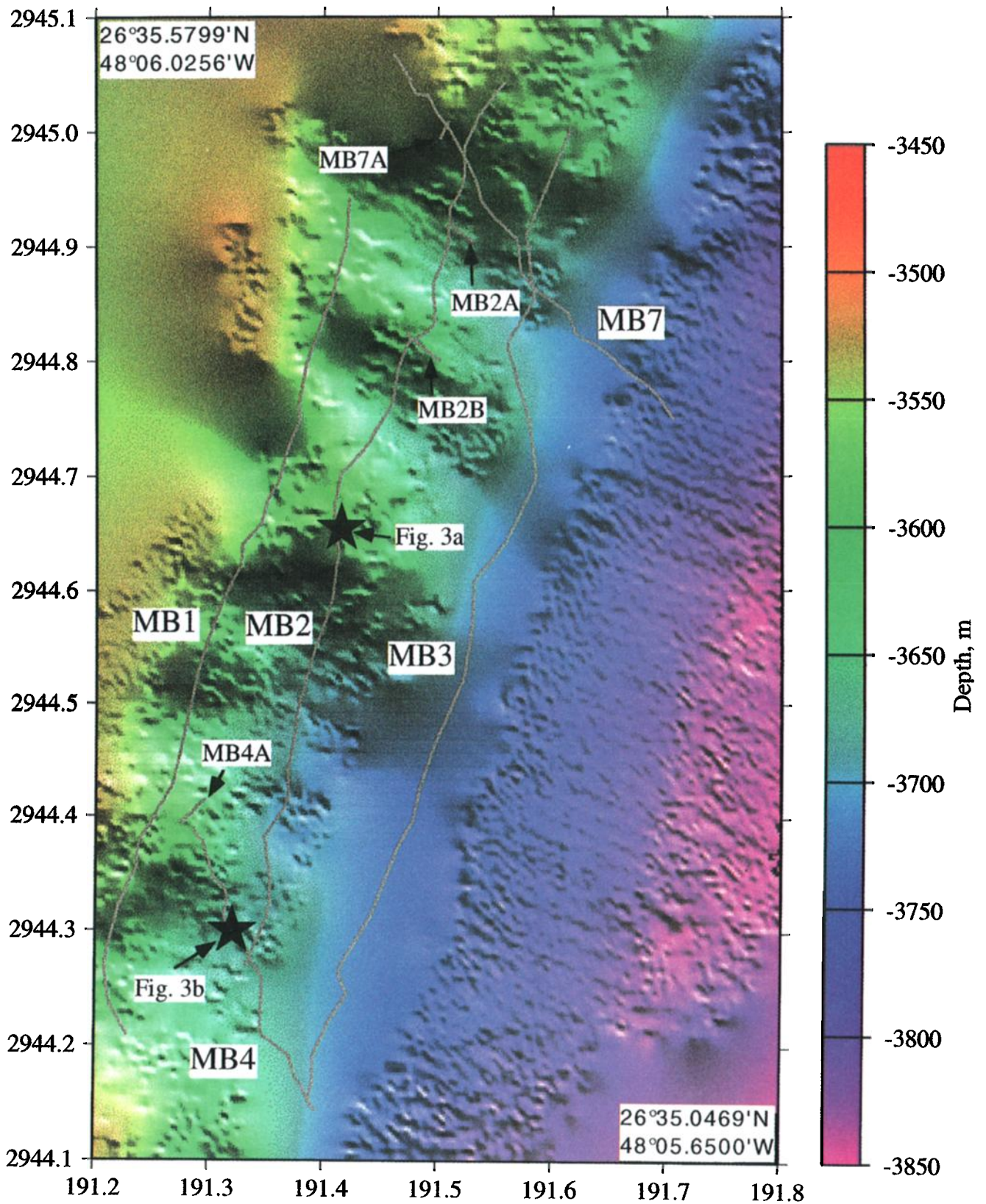
Plate 1b. Closeup of region boxed in Plate 1a, showing locations of Mesotech profiles used in this analysis. Very smooth areas in both plots are regions of interpolated data.
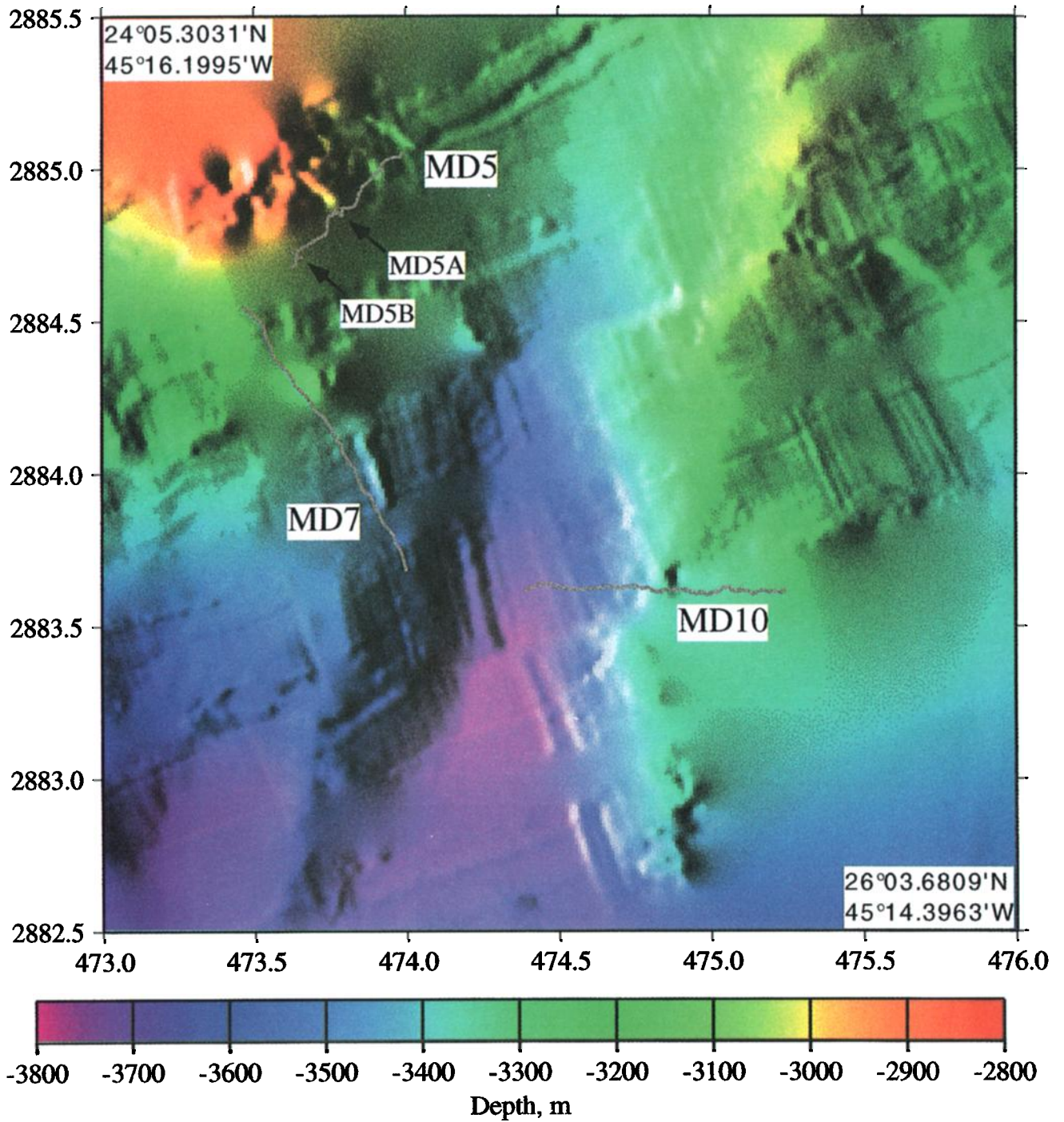
Plate 2. Color contoured, shaded relief image of gridded DSL-120 bathymetry at site D (see Figure 1). Box coordinates are in Universal Trans-Mercator units (km), and latitude and longitude of the upper left and lower right corners of the box are given. Artificial Sun illumination is from the west. Very smooth areas are regions of interpolated data.

sands of possible cross-track profiles are used (strike lines MB7A and MB4A; dip lines MB2A and MB2B); these cross-track profiles are a representative subset of those examined.

The three long Mesotech strike profiles (MB1 to MB3) roughly follow the upper, central, and lower part of a large, degraded fault scarp. MB1 is near the crest of the fault block, observed as flat-topped, resistant buttresses in Figure 4. Visual data show that these flat areas have thin, intermittent sediment cover, whereas the remainder of the profile crosses exposed basalt with sediment only in local, submeter-sized pockets. Profile MB2 at midscarp has similar basalt exposures but with sediment that is thick enough to cover the basalt on local flats and in the bottom of the two gullies in the northern part of the profile. Profile MB3 along the lower scarp has limited visual data; we infer from the visual and bathymetric data that the profile crosses dominantly exposed basalts, with probable sedimented talus on low slopes over the southern half of the profile. The steep slopes in cross-track, strike profiles MB4A and MB7A are exposed basalts, with some likely sediment cover on the flat block crest in profile MB7A (Figure 4).

Along-track dip profiles MB7 and MB4 (Figure 5) are all exposed basalt, except for the flat block crest in MB7, which is sedimented, and the low-gradient areas at the southeast ends of the profiles; these latter areas appear to be sedimented talus with local exposures of basaltic talus. The cross-track dip profiles, MB2B and MB2A, cross steep, mostly unsedimented basaltic scarps; sedimented talus probably occurs at the foot of the scarp in MB2A (Figure 5).

Hydrosweep strike and dip profiles HSB1 and HSB2 (Figure 1) were sampled from the gridded Hydrosweep data to coregister with Mesotech profiles MB1 and MB7, respectively. These and cross-track lines MB7A and MB2A (which roughly parallel strike and dip, respectively, but are not coregistered with the other profiles) are the basis for multiscale spectral analysis presented in the following section. The dip profile HSB2 is not centered on site B but rather extends west from the site. This was done to maintain statistical homogeneity; Goff et al. [1995] identified the region east of site B as one of lower rms height than site B or the region west of it.

Site D. Locations of site D Mesotech profiles analyzed are shown in Plate 2, superimposed on DSL-120 bathymetry. As already noted, there is no measurable anisotropic ratio to the bathymetry in this region [Goff et al., 1995], and that conclusion is supported by visual examination of the DSL-120 bathymetry. There are NNE and NE strikes on the local valley-bounding scarps noted earlier, but there are also scarps oriented to the east and SE.

At site D we do not differentiate the Mesotech profiles as strike or dip lines. The northernmost along-track profile, MD5, follows the lower part of an irregular NE trending scarp, crossing buttresses and gullies formed by faulting and mass wasting (Figure 6). Visual data show basalt outcrops on slopes, thinly sedimented basalt on elevated flats, and sedimented talus in low-gradient depressions. Line MD7 is orthogonal to MD5 and obliquely crosses an ENE striking ramp which probably consists mostly of thinly sedimented talus (no visual data are available
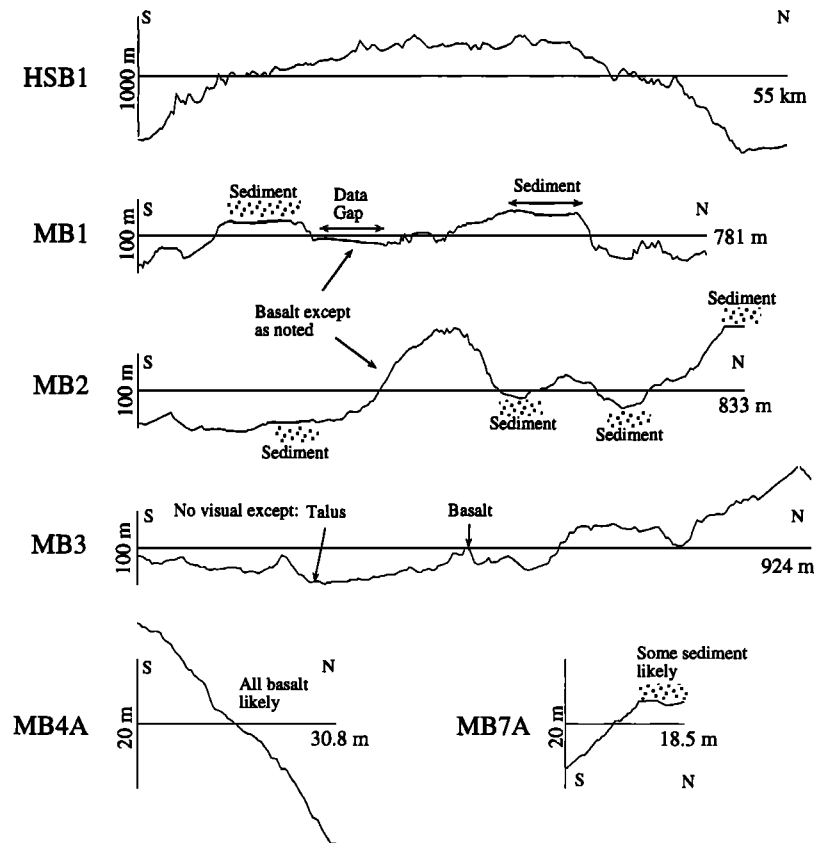

Figure 4. Site B strike profiles (locations in Plate 1b). Geologic annotations are based on video and photographic observations. The Hydrosweep profile is plotted at a vertical exaggeration of 10:1, and all others are plotted at 1:1.
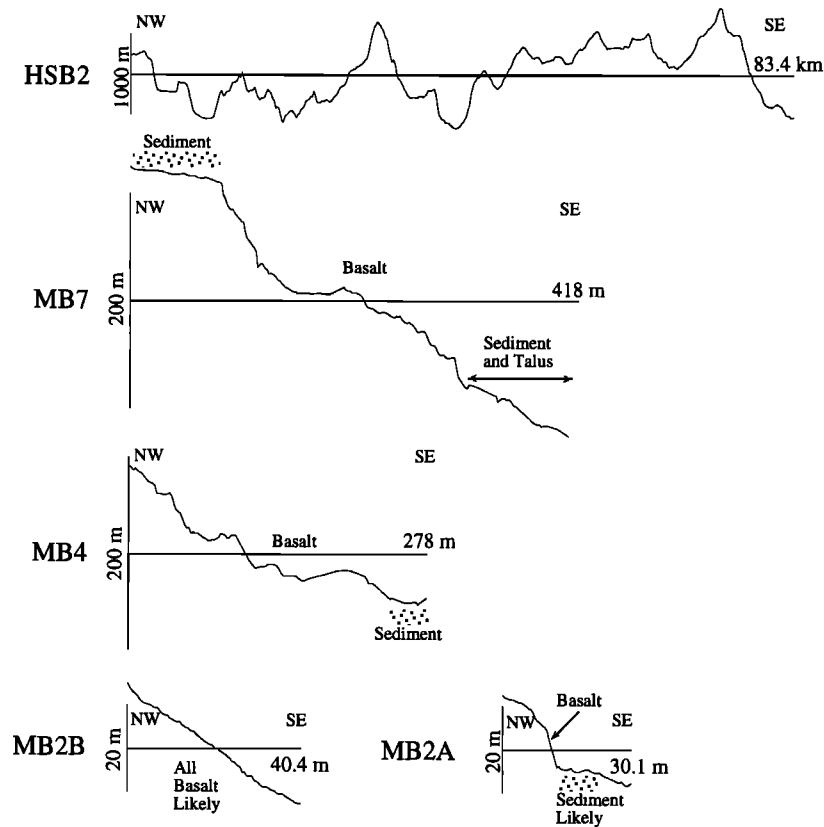
Figure 5. Site B dip profiles (locations in Plate 1b). Geologic annotations are based on video and photographic observations. The Hydrosweep profile is plotted at a vertical exaggeration of 10:1, and all others are plotted at 1:1.

along this profile). Line MD10 crosses a major NNE trending scarp consisting of exposed basalts, and thinly sedimented talus is observed at the foot of the scarp. The crest of this fault block is probably sediment-covered over the flats, with intermittent basalt exposures on the sloping seafloor. Two cross-track Mesotech profiles, MD5A and MD5B, were chosen in representative areas (Figure 6). The seafloor in MD5A is a ~35° ramp with lightly sedimented talus and possibly some basalt outcrops. Profile MD5B is a ~45° scarp consisting of basalt outcrops with probable local accumulation of sedimented talus.

Only one Hydrosweep profile was chosen for site D, HSD1 (Figure 1), which is coregistered with Mesotech line MD10. In any other orientation, a long Hydrosweep profile would quickly exit from inside-corner type morphology.

Sites A and C. Mesotech sampling at site A was more limited than at sites B and D. More importantly, site A has significantly thicker sediment cover (average ~40 m) and fewer sediment-free areas profiled by Mesotech. For this reason, we excluded site A Mesotech data from our analysis. Site C was not surveyed with the Mesotech, so it also is excluded from analysis.

Spectral Analysis of Profiles

Prior to spectral analysis, all profiles were detrended and the first and last 10% of each profile was tapered with a $\cos^2$ function. An fast Fourier transform (FFT) algorithm was then applied, and the resulting complex spectrum was squared to achieve a sample power spectrum (periodogram), which is an unbiased estimator (in the limit of large N) of the true power spectrum

[*Priestly*, 1981]. The results are plotted on $\log_{10}$-$\log_{10}$ plots. Spectral smoothing is not applied; we prefer instead to view the highly erratic periodogram and consider it as an empirically defined error envelope. Periodograms are presented as a function of linear wavenumber u (cycles per kilometer) rather than angular wavenumber ω (radians per kilometer) which is the direct product of the FFT. The two are related simply by $u = \omega/2\pi$.

Where appropriate, slope of the $\log_{10}$-$\log_{10}$ periodogram is estimated through a linear least-squares inversion [e.g., *Menke*, 1989], weighted by the inverse of the log periodogram data covariance:

$$\log_{10} P(u) = a + b[\log_{10}(u) - \log_{10}(u_0)], \tag{1}$$

where $P(u)$ is the periodogram and u_0 is a reference wavenumber. Hence a is the $\log_{10}$ periodogram estimate at reference value u_0, and b is the best fit slope. The fractal dimension D is calculated from the slope simply by [e.g., *Gilbert and Malinverno*, 1988]

$$D = \frac{5+b}{2}. \tag{2}$$

Periodogram samples are assumed to be uncorrelated [see *Priestley*, 1981] and the standard deviation in $\log_{10}$ space, which is estimated empirically, is assumed to be uniform.

In the multiscale spectral analysis we visually compare (without formal inversion) periodograms to the anisotropic von Kármán model presented by *Goff and Jordan* [1988]. In one-dimension, this is expressed as
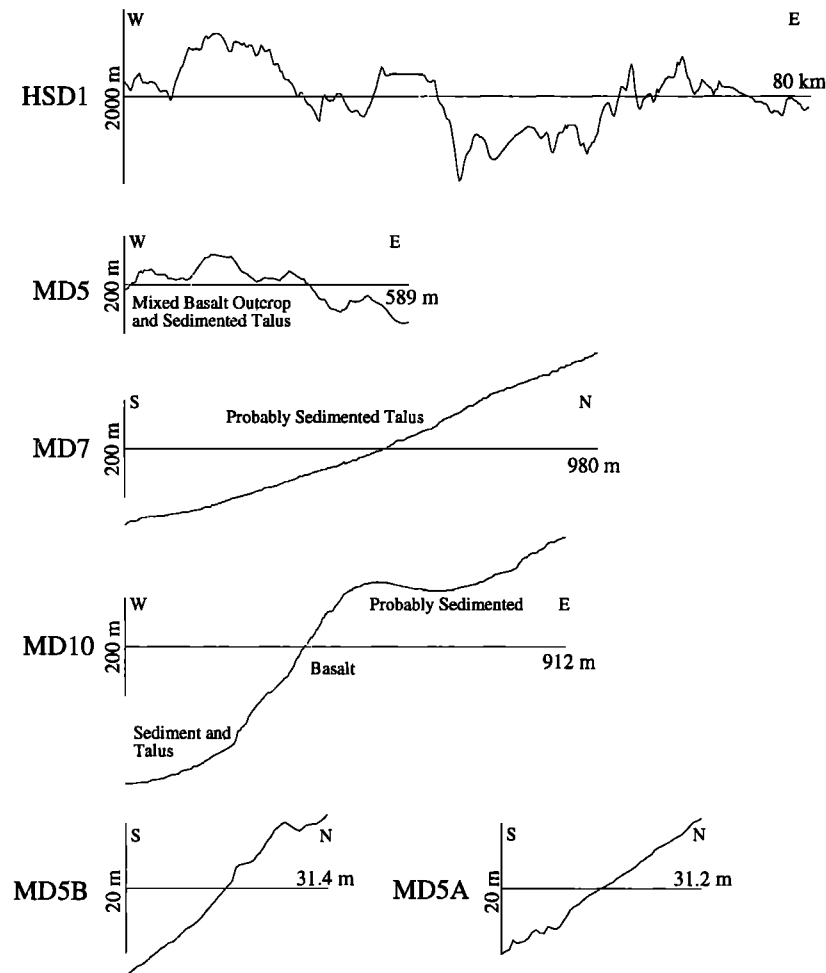
Figure 6. Site D profiles (locations in Plate 2). Geologic annotations are based on video and photographic observations. The Hydrosweep profile is plotted at a vertical exaggeration of 10:1, and all others are plotted at 1:1.

$$P(u) = \frac{\Gamma(v+1/2)}{\Gamma(v)} \frac{2H^2 \sqrt{\pi}(K_\theta / 2\pi)^{2v}}{[(K_\theta / 2\pi)^2 + u^2]^{v+1/2}},$$

(3)

$$K_\theta = \sqrt{(K_n \sin\theta)^2 + (K_s \cos\theta)^2}$$

where Γ is the gamma function, H is the rms height, K_s and K_n are corner wavenumbers in the strike and dip directions, respectively, θ is profile angle relative to strike, and v is the spectral roll-off ($D = 2 - v$, $b = 2v + 1$). Schematic representations of this function for the strike and dip directions are shown in Figure 2. For $u \gg K_\theta$, (3) is equivalent to (1).

Parameters of (3) in the vicinity of sites B and D were estimated from Hydrosweep data by *Goff et al.* [1995]. From a composite of several estimations, the following parameters for site B are adopted: $H = 245$ m, $K_n = 0.40$ km^{-1}, $K_s = 0.10$ km^{-1}, and lineament azimuth N25°E. At $\theta = 60°$, which is the azimuth of the site B dip profiles relative to the strike, $K_\theta = 0.35$. At site D there is no well-resolved lineament direction. The adopted parameters for that site are $H = 350$ m and $K_n = K_s = 0.24$ km^{-1}. A value of v was not well resolved in the estimation at either site; we rely on spectral analysis of the Mesotech data to derive that parameter.

Site B Analysis

Mesotech along-track lines: Estimation of fractal dimension. Analysis of site B profiles begins with straightforward estimation of the fractal dimension based on along-track Mesotech profiles. Periodograms are displayed in Figure 7 for Mesotech strike lines MB1 to MB3 and in Figure 8 for Mesotech dip lines MB4 and MB7. In both Figures 7 and 8, the envelopes of the displayed periodograms overlap closely, implying that the region we are sampling is statistically homogeneous (i.e., statistical properties do not change as a function of location). Also in Figures 7 and 8, the periodograms appear to closely follow a straight line, implying that over the range of scales sampled, a single fractal-dimension representation is appropriate. One minor exception, however, occurs at the highest wavenumbers where a flattening of the periodogram is observed (especially evident in MB1, Figure 7, among the strike profiles). This is likely attributable to noise in the bathymetric profile.

A straight line is fit as described above to the combined $\log_{10}$ periodogram sets in Figures 7 and 8. To remove the effect of noise, the periodograms are clipped at $\log_{10}(u) = 2.0$ for the strike periodograms (Figure 7) and at $\log_{10}(u) = 2.2$ for the dip periodograms (Figure 8). A reference wavenumber of $\log_{10}(u_0) = 1$ is used. For the combined strike spectra the estimated parameters are $a = -0.13 \pm 0.06$ and $b = -2.46 \pm 0.08$ (or $D = 1.27 \pm 0.04$),
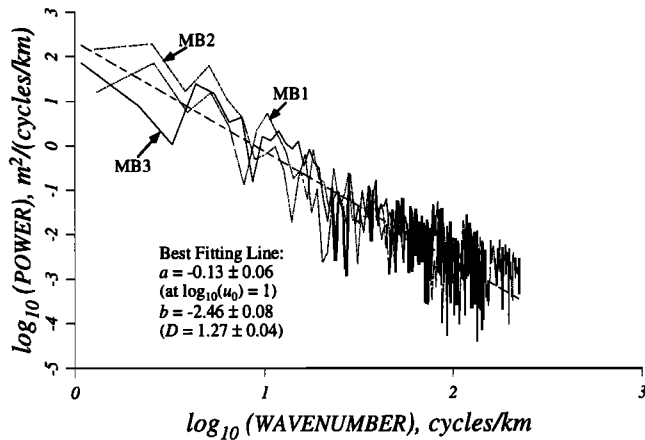
Figure 7. Site B strike periodograms from along-track Mesotech profiles, plotted in $\log_{10}$-$\log_{10}$ space, with best fit line for wavenumbers $<\log_{10}(u) = 2.0$.

Figure 9. Site B Hydrosweep (HSB2), Mesotech along-track (MB7), and Mesotech cross-track (MB2A) periodograms for the dip direction, plotted in $\log_{10}$-$\log_{10}$ space, with von Kármán model overlaid.

and for the dip spectra $a = -0.14 \pm 0.12$ and $b = -2.44 \pm 0.14$ ($D = 1.28 \pm 0.07$); strike and dip spectra are essentially identical. Hence the statistical model (Figure 2) is not entirely correct: while it does predict identical fractal dimensions in all directions, it does not predict identical power.

Multiscale analysis and comparison to power spectrum model. Figures 9 and 10 display Hydrosweep, Mesotech along-track, and Mesotech cross-track periodograms for the dip and strike directions, respectively. A von Kármán model power spectrum is overlaid corresponding to parameters $D = 1.27$, $H = 245$ m, $K_{\theta=60°} = 0.35$ km^{-1} (Figure 9) and $K_s = 0.10$ km^{-1} (Figure 10). On the dip periodograms (Figure 9), the model power spectrum matches well the corner wavenumber evident in the Hydrosweep periodogram (HSB2) and the entire length of the Mesotech along-track periodogram (MB7). However, the model mismatches by ~1 order of magnitude in power the high-wavenumber regions of the Hydrosweep periodogram. This mismatch is to be expected. The Hydrosweep profile HSB2 crosses many abyssal hill peaks and valleys and thus samples many sedimented depressions. The Mesotech lines, however, are almost entirely on exposed basement. As demonstrated numerically by *Webb and Jordan* [1993], pelagic sedimentation will
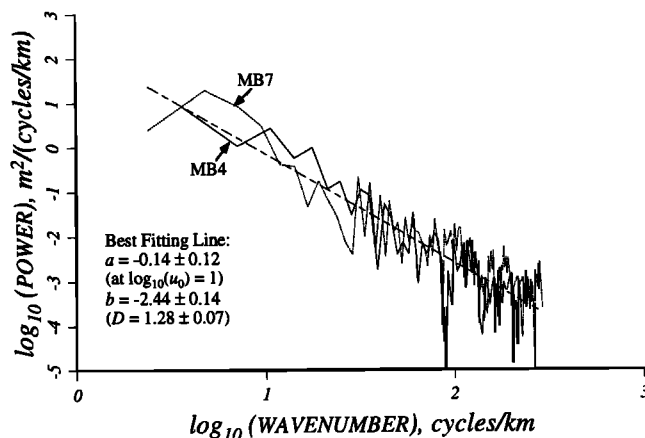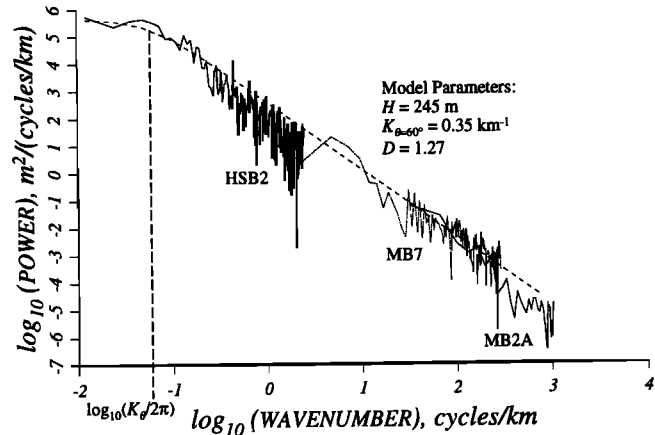
tend to dampen the higher-wavenumber component of bathymetry and reduce the fractal dimension. We can also demonstrate this effect empirically. The eastward extension of line MB7 continues over a large sediment pond. Periodograms from this heavily sedimented portion of the profile (not illustrated) are reduced in power by ~2.5 orders of magnitude at all Mesotech scales relative to the basement outcrop profiles. It is highly likely, therefore, that the mismatch between the Hydrosweep and Mesotech periodograms in this wavenumber region is simply an effect of sedimentation.

Although the model power spectrum matches the along-track Mesotech periodogram MB7, it mismatches the Mesotech cross-track periodogram (MB2A, Figure 9) at the highest wavenumbers. The fractal dimension exhibited by the MB2A periodogram is $D = 1.04 \pm .13$ (not resolvably different from 1.0, the minimum possible fractal dimension). Thin sediments are likely present above and below the small scarp evident on profile MB2A (Figure 5), and they are a possible explanation for the change in fractal behavior. However, as shall be discussed below, all periodograms examined from cross-track Mesotech profiles over basement exposures are nearly identical in the range $\log_{10}(u) \cong 2.5$-3, whether lightly dusted with sediments or entirely bare.
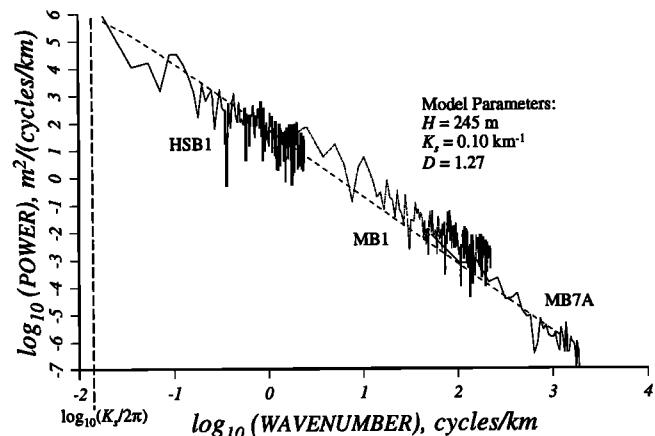

Figure 8. Site B dip periodograms from along-track Mesotech profiles, plotted in $\log_{10}$-$\log_{10}$ space, with best fit line for wavenumbers $<\log_{10}(u) = 2.2$.

Figure 10. Site B Hydrosweep (HSB1), Mesotech along-track (MB1), and Mesotech cross-track (MB7A) periodograms for the strike direction, plotted in $\log_{10}$-$\log_{10}$ space, with von Kármán model overlaid.

Also, visual examination of thinly sedimented seafloor within the survey area (Figure 3) suggests that sediments will not be a significant factor at the resolution scale of the Mesotech instrument (~0.5 m). We conclude that there likely exists a true change in fractal behavior of basement morphology at the smallest scales of our survey.

In the strike direction (Figure 10), the corner wavenumber is not evident on either the model or the Hydrosweep periodogram (HSB1) because the corner wavelength (~63 km) is too large to be sampled with the HSB1 profile length of 55 km. The model spectrum in the strike direction generally represents a very poor match to the strike periodograms. The HSB1 slope is surprisingly gradual (fractal dimension of $1.46 \pm .06$). HSB1 should not be strongly affected by sediments because it runs along the spine of a large abyssal hill and has only local, thin sediment cover. The model slope does match the slope of the Mesotech along-track periodogram (MB1), but it underestimates its power by ~1 order of magnitude. The model also does not match the slope of the cross-track periodogram (MB7A), from which we estimate a very low fractal dimension of 0.98 ± 0.13 (also not resolvably different from 1.0).

The along-strike spectral properties at site B thus exhibit three distinct fractal regimes at wavenumbers higher than the corner wavenumber: from the corner wavenumber $u = K_s/2\pi$ to $\log_{10}(u) \cong 0.5$ with fractal characterization $\cong 1.46$, from there to $\log_{10}(u) \cong 2$ with fractal characterization $\cong 1.27$, and at higher wavenumbers with a fractal characterization $\cong 1.0$. (The wavenumbers identified here as transitions in fractal character represent our best estimates. However, due to the erratic nature of the periodogram, an error range of $\pm$ ~0.5 order of magnitude is possible.)

The cross-track Mesotech periodograms displayed thus far in both strike and dip directions are nearly identical. The MB7A periodogram has an estimated power at $\log_{10}(u_0) = 2$ of -2.88 $\pm$ 0.24, and the MB2A periodogram has an estimated power of -2.59 $\pm$ 0.19 at the same reference wavenumber (the 1-σ error on the difference, $\sqrt{0.24^2 + 0.19^2} = 0.30$, is greater than the difference). Furthermore, both periodograms exhibit a fractal dimension indistinguishable from 1.0. The same similarity occurs between periodograms for along-track strike and dip profiles (Figures 7 and 8). Thus, the spectral properties of the basement morphology at site B appear to be direction-invariant over the all Mesotech scales (< ~0.5 km).

Conceptual model. To summarize our observations up to this point, we present a new conceptual model for the power spectrum of abyssal hill basement morphology (Figure 11). As with the earlier model (Figure 2), the strike and dip directions have distinctly different corner wavenumbers; this is how abyssal hill lineaments, obvious to the eye, are characterized in the statistical model. At higher wavenumbers, the strike power spectrum decreases gradually (a high fractal characterization of ~1.46), while the dip power spectrum decreases more rapidly (a moderate fractal characterization of ~1.27). The strike and dip power spectra meet at $\log_{10}(u) \cong 0.5$, where they remain identical with a fractal dimension of ~1.27. At $\log_{10}(u) \cong 2$, the spectral slope steepens to a fractal characterization of ~1.0.

A closer look at the finest scales. The cross-track Mesotech profiles used for spectral analysis in Figures 9 and 10 (lines MB2A and MB7A respectively) are not representative of all such profiles sampled. These particular examples cross small, steep scarps or slope breaks (Figures 4 and 5), whereas many other profiles, such as MB4A and MB2B (Figures 4 and 5, respectively),
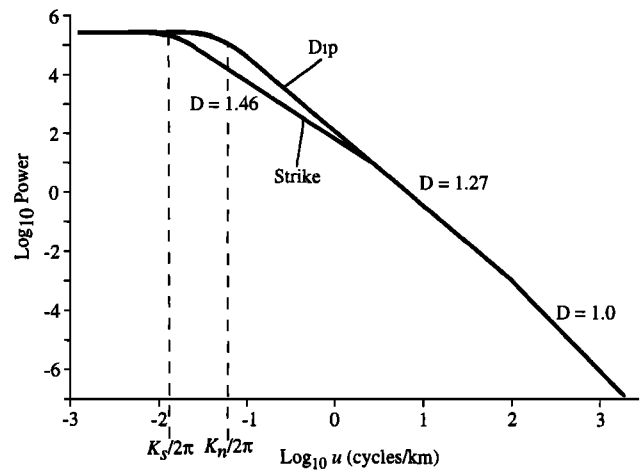

Figure 11. New conceptual model for the abyssal hill basement power spectrum.

do not. Figure 3 presents such a contrast with still images. Figure 3a shows a steep slope that is otherwise featureless except for a cobble-like roughness at the ~10-20 cm scale (too small to be seen in the Mesotech profiles). By contrast, Figure 3b displays a sharp break in slope at the base of a steep slope.

The differences in periodograms of profiles MB2A (with slope breaks) and MB2B (without slope breaks) are striking. In Figure 12 these periodograms are plotted along with the periodogram for the along-track line MB7 (all are in the dip direction). At the largest wavenumbers (> ~$\log(u) \cong 2.5$) the MB2A and MB2B periodograms are nearly identical, but at lower wavenumbers they diverge up to almost 2 orders of magnitude in power.

Lines MB2A and MB2B represent extrema in the range of small-scale periodograms observed. Figure 13 displays a suite of best fit lines for all the cross-track Mesotech periodograms presented in Figures 4-6 (profiles for site D are included because the small-scale behavior there is the same). A wide divergence is observed at the lower wavenumbers of these periodograms (up to 2 orders magnitude power), but they converge at higher wavenumbers. Comparison with Figures 4-6 indicates that those profiles whose periodograms exhibit greater power at lower wavenumber contain a significant break in slope.
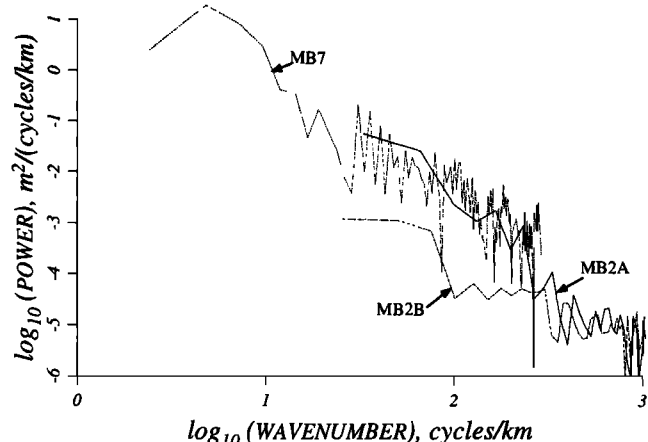

Figure 12. Periodograms for site B cross-track Mesotech lines, one of which crosses a small scarp (MB2A) and one of which does not (MB2B). Also shown is periodogram for along-track Mesotech line MB7.
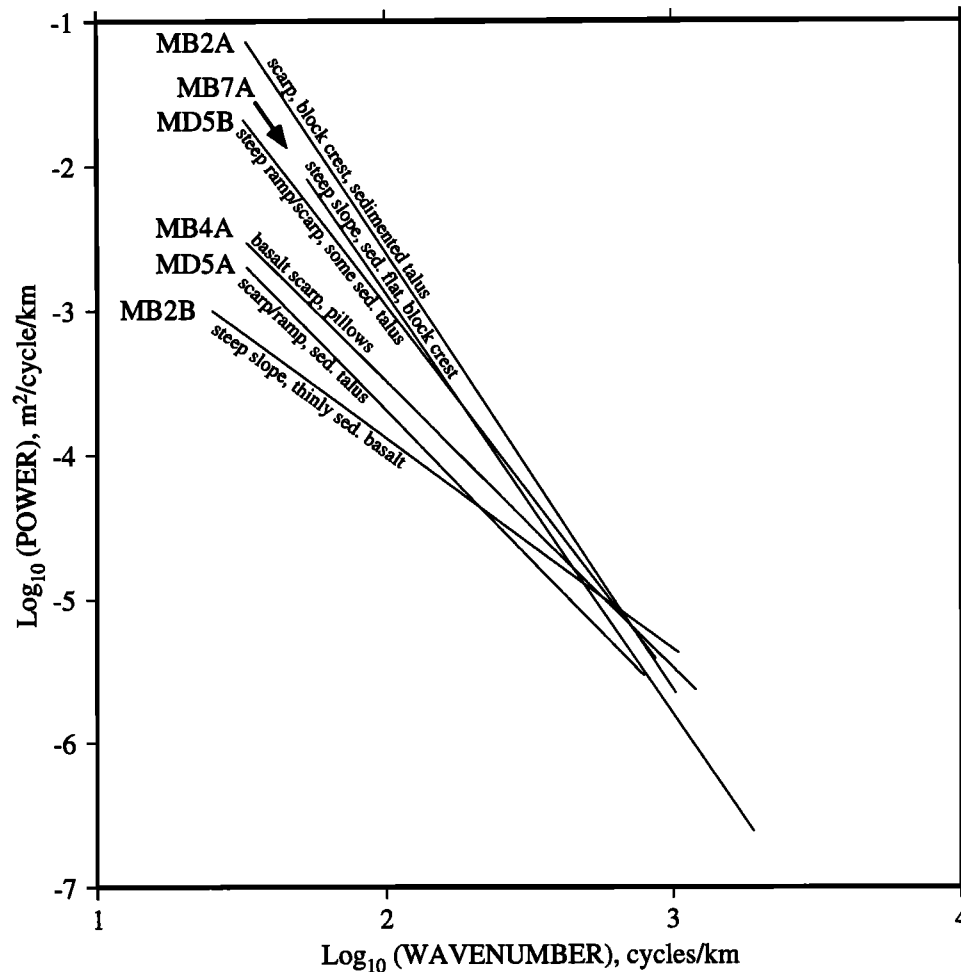
Figure 13. Best fit lines for all cross-track Mesotech periodograms used in this analysis.

To summarize, sometimes a cross-track Mesotech profile includes a significant slope break, and sometimes it does not; unless it does, its periodogram cannot be reconciled with that of the longer and more coarsely sampled along-track profiles (this is also true at site D, the full analysis of which is presented below). This result demonstrates a breakdown in the self-affine (i.e., simple fractal) nature of the morphology, i.e., that morphology observed at small scales cannot be described as a simple fractal extrapolation of what is observed at large scales. In particular, significant slope breaks do not occur at all scales. Because Mesotech cross-track profiles do not always capture significant slope breaks, we conclude that the minimum spacing between such breaks is larger than the typical Mesotech swath width (~20-50 m).

Site D Analysis

Along-track mesotech profiles: A fractal analysis. As at site B, analysis of site D begins with a fractal characterization of the along-track Mesotech profiles. Periodograms for profiles MD5, MD7, and MD10 (Plate 2 and Figure 6) are displayed in Figure 14. We first note that the periodogram for MD7 has significantly less power and higher fractal characterization than the periodograms for MD5 and MD10. For MD7 we estimate a fractal characterization of D = 1.44 ± 0.05 and amplitude a = -1.24 ± 0.09 at $\log_{10}(u_0)$ = 1, while for combined periodograms MD5

and MD10 we estimate D = 1.15 ± 0.05 and a = -0.25 ± 0.08 at the same reference wavenumber. Note that the differences in periodograms are manifest only at the lower wavenumbers (< $\log_{10}$ (u) ≅ 1.5). As stated earlier, line MD7 appears to sample entirely a talus slope. We thus conclude, not surprisingly, that talus smooths intermediate-scale (~25 m to ~1 km) morphology.

The estimated fractal characterization of MD5 and MD10 (D = 1.15 ± 0.05) differs significantly from that of site B, where D = 1.27 ± 0.04 for strike periodograms and D = 1.28 ± 0.07 for dip periodograms. The best fitting lines for site D (lines MD5 and MD10 only) and site B periodograms intersect at $\log_{10}(u)$ ≅ 0.69, or wavelength ≅ 0.2 km (Figure 14). Thus, at scales larger than ~0.2 km, site D has larger features, whereas at scales smaller than ~0.2 km, site B has larger features. However, owing to the change in fractal character noted before at site B for wavenumbers greater than $\log_{10}(u)$ ≅ 2 (wavelengths < ~10 m), the periodograms at the two sites converge by $\log_{10}(u)$ ≅ 2.5. As noted on Figure 13, there is no discernible difference in the periodograms of the cross-track Mesotech lines at sites B and D.

Multiscale spectral analysis. Periodograms for Hydrosweep (HSD1), along-track Mesotech (MD10), and cross-track Mesotech (MD5A) profiles for site D are shown in Figure 15. Again, we have overlaid a von Kármán model using the fractal dimension estimated from the along-track Mesotech periodogram (~1.15) and the corner wavenumber derived from the Hydrosweep data [Goff et al., 1995] (K_n = K_s = ~0.24 km⁻¹). As be-
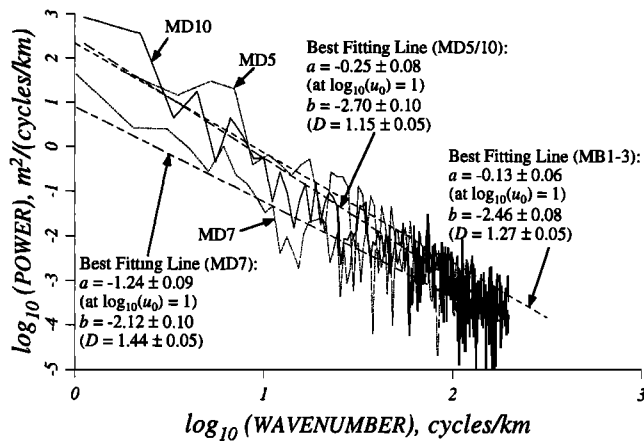
Figure 14. Site B periodograms from along-track Mesotech profiles, plotted in $\log_{10}$-$\log_{10}$ space, with best fit lines (separate estimations are provided for line MD7 and for combined lines MD5 and MD10).

fore, we find some misfit, though small in this case, between the model power spectrum and the higher wavenumbers of the Hydrosweep periodogram, probably because of sediment accumulation. Sedimentation effects at site D are likely less than at site B because site D is young crust with average sediment thickness which is lower by a factor of ~4-5. Aside from that, the model power spectrum fits the periodograms remarkably well at all scales. In particular, there is no obvious change in fractal behavior at the smallest scales, provided that the cross-track Mesotech profile crosses a significant slope break.

Discussion and Conclusions

Using both sea surface multibeam and near-bottom, fine-scale bathymetric data, we have examined the power spectra of Mid-Atlantic Ridge flank topography across scales ranging from tens of kilometers down to ~1 m. To the extent permitted by the data, our analyses focus on unsedimented to thinly sedimented crust. Thus the spectral properties are considered to be generally representative of the surficial structure of oceanic basement in a slow
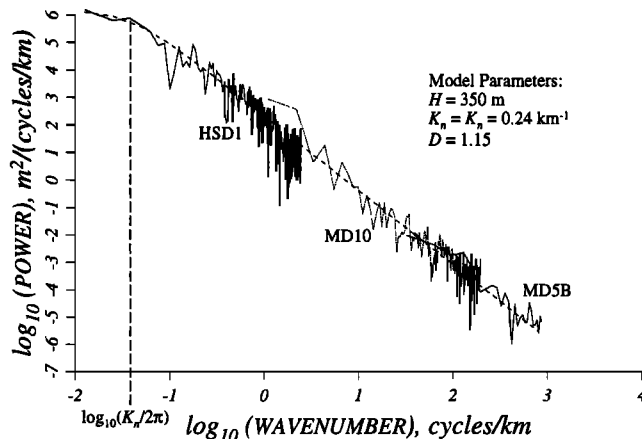

Figure 15. Site D Hydrosweep (HSD1), Mesotech along-track (MD10), and Mesotech cross-track (MD5B) periodograms, plotted in $\log_{10}$-$\log_{10}$ space, with von Kármán model overlaid.

spreading environment. We find that the spectral properties of basement morphology are only partially consistent with anisotropic von Kármán model (Figure 2) proposed by *Goff and Jordan* [1988]. In the following, we present our primary conclusions along with interpretation within the context of the geological processes which most likely have shaped and modified basement topography.

A New Statistical Model: Effects of Mass Wasting on Abyssal-Hill Morphology

The site B (outside-corner setting) strike and dip spectra are identical at wavenumbers greater than $\log_{10}(u) \cong 0.5$ (~0.3 km wavelength). In the $\theta = 60°$ "dip" direction, the statistical properties of abyssal hill topography (taking into account the likely effects of sediment smoothing) are consistent with a von Kármán power spectrum model down to ~$\log_{10}(u) \cong 2$ (wavelength $\cong$ 10 m), with model parameters $H \cong 245$ m, $K_\theta \cong 0.35$ km^{-1}, and $D \cong 1.27$. The site B along-strike statistical properties are more complex: a smaller corner wavenumber ($K_s \cong 0.10$ km^{-1}) is observed, as expected, but we also find a larger fractal characterization (~1.46) in the region between the corner wavenumber ($u = K_s/2\pi$) and $\log_{10}(u) \cong 0.5$, where the dip and strike periodograms merge (Figure 11).

The site D (inside-corner setting) spectra are generally consistent with a von Kármán statistical model over all scales observed (taking into account the likely effects of sediment smoothing, and provided a significant slope break is sampled at the smallest scales), with parameters $H \cong 350$ m, $K_n = K_s \cong 0.24$ km^{-1}, and $D \cong 1.15$. This fractal dimension is resolvably different from that observed on along-track Mesotech periodograms at site B.

We suggest that convergence of strike and dip spectra observed at site B at wavenumbers $>\log_{10}(u) \cong 0.5$ may be related to mass wasting of the ocean crust. If true, this is the first quantitative characterization of this process. This mass wasting, in the form of canyon cutting, slumps and slides, tends to occur orthogonal to the strike of fault scarps and abyssal hills [*Tucholke, et al.*, 1997a]. The canyons are of the order of a few hundred meters wide. Mass wasting therefore adds seafloor roughness along strike at wavelengths of a few hundred meters and less, which is consistent with the range of scales where the strike and dip periodograms merge. At the same time, the cross-strike roughness may be reduced by the formation of relatively smooth talus ramps (e.g., Figure 14). Thus, starting from an idealized von Kármán power spectrum model (Figure 2), we speculate that mass wasting will increase the power of the strike periodogram over wavenumbers $>\log_{10}(u) \cong 0.5$, which would necessarily lower the spectral slope (increase the apparent fractal dimension) at smaller wavenumbers. In addition, we may see some decrease in the power of the dip periodogram over the same scales. The result would be a morphology which, at the smaller scales affected by mass wasting, would exhibit little if any structural anisotropy .

The difference in fractal dimension between sites B and D is associated both with greater large-scale ($>$~200 m) roughness and less intermediate-scale ($<$~200 m and $>$~10 m) roughness at site D relative to site B (Figure 14). We can attribute the observation of greater large-scale roughness at site D to differences in abyssal hill faulting at IC and OC settings [*Goff et al.*, 1995]. Less intermediate scale roughness at site D, a new observation, may also be related to the difference in IC and OC settings; the IC crust at site D may be missing much of its volcanic carapace [e.g.,

Tucholke and Lin, 1994] and thus have less volcanic, intermediate-scale roughness than the OC setting at site B. However, sites B and D are both dominantly scarp regions, with few if any undisturbed volcanic constructs actually observed. Thus the differences between sites B and D intermediate-scale roughness may instead be related to different degrees of mass wasting. Site B is on mature (~24 Ma) crust, and fault scarps there are pervasively incised by mass wasting. Site D, on the other hand, is on young crust (~3 Ma), and scarps there are only moderately modified by mass wasting. As suggested above, mass wasting should tend to increase roughness at wavenumbers $>\log_{10}(u) \cong 0.5$, and thus be a significant factor leading to greater intermediate-scale roughness at site B than at site D. Our analyses, however, cannot definitively say that the difference in roughness at the two sites reflects a significant continuation of mass wasting beyond 3 Ma; it is also possible that OC crust is simply more susceptible to mass wasting than IC crust.

Smallest Scales: A Change in Fractal Behavior

The periodograms estimated from the Mesotech cross-track profiles at both sites B and D are highly variable at their low-wavenumber end (~1.5 $\leq \log_{10}(u) \leq$ ~2.0) (Figure 13), overlapping with the high-wavenumber end of along-track Mesotech periodograms only when the cross-track profile crosses a significant slope break (Figure 12). Because the scarps and slope breaks which contribute power in the low-wavenumber part of the cross-track Mesotech periodograms are present only occasionally on the short profiles, we conclude that such features, which principally represent crustal dissection by faulting and slope failure, are spaced no more closely than the typical Mesotech swath width of ~20-50 m. The variability of Mesotech cross-track spectra also implies a fundamental change in the fractal nature of basement morphology at small scales. A fractal field is also self-affine [*Mandelbrot*, 1983], meaning that, with appropriate scaling, a small piece of the field looks statistically identical to a larger piece. The observed spectral variability implies that self-affinity breaks down where a minimum spacing in significant slope breaks is reached. Correlatively, self-affinity at larger scales suggests that significant slope breaks, i.e., crustal dissection by faulting and slope failure, are the fundamental controls on abyssal hill basement morphology at scales larger than a few tens of meters. However, this study does not adequately investigate the contribution of volcanic morphology so we cannot discount it as an important factor.

Despite their low-wavenumber variability, the Mesotech cross-track periodograms all tend to converge near wavenumber $\log_{10}(u) \cong 2.7$ (~2.0 m wavelength) (Figure 13). This new and perhaps surprising observation suggests that at scales of a few meters or less, the crustal roughness is very similar at both young and old sites and at both inside- and outside-corner crust. In other words, the roughness engendered by boulders, basaltic pillows, joints, cracks, and so forth, seems to be roughly similar over all crust observed.

Part of the original impetus for this study was to assess the character of fine-scale roughness as a control for acoustic scattering studies, and in this regard our observations on the breakdown of self affinity at the smallest scales have two important implications (See *Goff* [1995] for additional discussion and references): (1) Basement morphology can be described physically in terms of a composite roughness model [e.g., *McDaniel and Gorman*, 1983], that is as relatively smooth, diffusely scattering

fine-scale roughness superimposed on larger-scale morphology which reflects specularly (here with a separation scale of tens of meters). Composite roughness assumptions allow for approximations which make analytic computations of scattering from complex surfaces tractable. A simple fractal morphology is not obviously separable into two scale regimes, although composite roughness assumptions have been applied in such cases [*Jackson et al.*, 1986]. (2) Scarps and other surfaces are smooth enough that they can likely be considered as reflecting facets (depending on the acoustic wavelength) [e.g., *Gerstoft and Schmidt*, 1991]. Facet models are used to model the occurrence of bright reflectors, or glinting.

Sediment Smoothing: Quantitative Constraints

Sedimentation has two observable effects: (1) in a mismatch between Hydrosweep and along-track Mesotech periodograms (Figures 9 and 15), and (2) in a difference in power between along-track Mesotech periodograms from profiles over heavily sedimented region and profiles over basement outcrop (the former exhibit 2.5 orders of magnitude less power). A comparison of Hydrosweep periodograms in Figures 9 and 15 shows how sediments smooth basement roughness. The site D profile samples terrain only marginally affected by sediments (<6 m average thickness), and the difference between its periodogram and the von Kármán model is minor and occurs only at the highest wavenumbers (Figure 15). By contrast, the site B Hydrosweep dip profile covers more sedimented terrain (~30 m average thickness), and its periodogram deviates much more significantly from the von Kármán model (Figure 9). In the latter case, the difference between model and observation increases with increasing wavenumber. We interpret this as a quantitative demonstration that sedimentation affects seafloor morphology in a progressive manner, smoothing first the smaller scales and later affecting larger scales. This conclusion is consistent with numerical-based predictions of sediment smoothing derived by *Webb and Jordan* [1993], and it thus provides observational support for the validity of their model.

References

Bell, T. H., Statistical features of sea-floor topography, *Deep Sea Res.*, *22*, 883–892, 1975.

Bemis, K. G., and D. K. Smith, Production of small volcanoes in the superswell region of the south Pacific, *Earth Planet. Sci. Lett.*, *118*, 251-262, 1993.

Bicknell, J. D. J.-C. Sempere, K. C. Macdonald, and P. J. Fox, Tectonics of a fast spreading center: A Deep-Tow and Sea Beam survey on the East Pacific Rise at 19°30'S, *Mar. Geophys. Res.*, *9*, 25-45, 1987.

Carbotte, S. M., and K. C. Macdonald, Comparison of seafloor tectonic fabric at intermediate, fast, and super fast spreading ridges: Influence of spreading rate, plate motions, and ridge segmentation on fault patterns, *J. Geophys. Res.*, *99*, 13,609-13,631, 1994.

Cowie, P. A., A. Malinverno, W. B. F. Ryan, and M. H. Edwards, Quantitative fault studies on the East Pacific Rise: A comparison of sonar imaging techniques, *J. Geophys. Res.*, *99*, 15,205-15,218, 1994.

Dick, H. J. B., G. Thompson, and W. B. Bryan, Low-angle faulting and steady state emplacement of plutonic rocks at ridge-transform intersections (abstract), *Eos Trans. AGU*, *62*, 406, 1981.

Edwards, M. H., D. J. Fornari, J. A. Madsen, A. Malinverno, and W. B. F. Ryan, Evaluating plate tectonic predictions using SeaMARC II data for the East Pacific Rise, *J. Geophys. Res.*, *96*, 7995-8017, 1991.

Fox, C. G., and D. E. Hayes, Quantitative methods for analyzing the roughness of the seafloor, *Rev. Geophys.*, *23*, 1-48, 1985.

Gerstoft, P., and H. Schmidt, A boundary element approach to ocean seismoacoustic facet reverberation, *J. Acoust. Soc. Am.*, *89*, 1629-1642, 1991.

Gilbert, L. E., and A. Malinverno, A characterization of the spectral density of residual ocean floor topography, *Geophys. Res. Lett.*, *15*, 1401-1404, 1988.

Goff, J. A., The relationship between local- and global-scale scattering functions for fractal surfaces under a separation of scales hypothesis, *J. Acoust. Soc. Am.*, *97*, 1586-1595, 1995.

Goff, J. A., and T. H. Jordan, Stochastic modeling of seafloor morphology: Inversion of Sea Beam data for second-order statistics, *J. Geophys. Res.*, *93*, 13,589-13,608, 1988.

Goff, J. A., and M. C. Kleinrock, Quantitative comparison of bathymetric survey systems, *Geophys. Res. Lett.*, *81*, 1253-1256, 1991.

Goff, J. A., B. E. Tucholke, J. Lin, G. E. Jaroslow, and M. C. Kleinrock, Quantitative analysis of abyssal hills in the Atlantic Ocean: A correlation between inferred crustal thickness and extensional faulting, *J. Geophys. Res.*, *100*, 22,509-22,522, 1995.

Herzfeld, U. C., I. I. Kim, and J. A. Orcutt, Is the ocean floor a fractal?, *Math. Geol.*, *27*, 421-462, 1995.

Jackson, D. R., D. P. Winebrenner, and A. Isharu, Application of the composite roughness model to high frequency bottom backscattering, *J. Acoust. Soc. Am.*, *79*, 1410-1422, 1986.

Karson, J. A., Seafloor spreading on the Mid-Atlantic Ridge: Implications for the structure of ophiolites and oceanic lithosphere produced at slow spreading environments, in *Proceedings of the Symposium TROODOS 1987*, edited by J. Malpas et al., pp. 547-555, Geol. Surv. Dep., Nicosia, Cyprus, 1990.

Karson, J. A., and H. J. B. Dick, Tectonics of ridge-transform intersections at the Kane Fracture Zone, *Mar. Geophys. Res.*, *6*, 51-98, 1983.

Krause, D. C., and H. W. Menard, Depth distribution and bathymetric classification of some seafloor profiles, *Mar. Geol.*, *3*, 169-193, 1965.

Lonsdale, P., Structural geomorphology of a fast-spreading rise crest: The East Pacific Rise near 3°25'S, *Mar. Geophys. Res.*, *3*, 251-293, 1977.

Mandelbrot, B. B., *The Fractal Geometry of Nature*, 468 pp., W. H. Freeman, New York, 1983.

McDaniel, S. T., and A. D. Gorman, An examination of the composite-roughness scattering model, *J. Acoust. Soc. Am.*, *73*, 1476-1486, 1983.

McDonald, M. F., and E. J. Katz, Quantitative method for describing the regional topography of the ocean floor, *J. Geophys. Res.*, *74*, 2597-2607, 1969.

Menke, W., *Geophysical Data Analysis: Discrete Inverse Theory*, Int. Geophys. Ser.s, vol. 45, Academic, San Diego, Calif., 1989.

Neidell, N. S., Spectral studies of marine geophysical profiles, *Geophysics*, *31*, 122-134, 1966.

Priestly, M. B., *Spectral Analysis and Time Series*, 890 pp., Academic, San Diego, Calif., 1981.

Robertsson, J. O. A., A. Levander, and K. Holliger, A hybrid wave propagation simulation technique for ocean acoustic problems, *J. Geophys. Res.*, *101*, 11,225-11,241, 1996.

Severinghaus, J. P., and K. C. Macdonald, High inside corners at ridge-transform intersections, *Mar. Geophys. Res.*, *9*, 353-367, 1988.

Smith, D. K., and J. R. Cann, Building the crust at the Mid-Atlantic Ridge, *Nature*, *365*, 707-715, 1993.

Smith, D. K., and T. H. Jordan, Seamount statistics in the Pacific Ocean, *J. Geophys. Res.*, *93*, 2899-2917, 1988.

Tucholke, B. E., and J. Lin, A geologic model for the structure of ridge segments in slow spreading ocean crust, *J. Geophys. Res.*, *99*, 11,937-11,958, 1994.

Tucholke, B. E., K. C. Macdonald, and P. J. Fox, ONR seafloor natural laboratories on slow- and fast-spreading mid-ocean ridges, *Eos Trans. AGU*, *72*, 268-270, 1991.

Tucholke, B. E., W. K. Stewart, and M. C. Kleinrock, Long-term denudation of ocean crust in the central North Atlantic Ocean, *Geology*, *25*, 171-174, 1997a.

Tucholke, B. E., J. Lin, M. C. Kleinrock, M. A. Tivey, T. B. Reed, J. A. Goff, and G. E. Jaroslow, Segmentation and crustal structure of the western Mid-Atlantic Ridge flank, 25°30'-27°10'N and 0-29 m.y., *J. Geophys. Res.*, in press, 1997b.

Webb, H. F., and T. H. Jordan, Quantifying the distribution and transport of pelagic sediments on young abyssal hills, *Geophys. Res. Lett.*, *20*, 2203-2206, 1993.

Yesyunin, R. Y., Description of bottom relief by means of the spatial correlation function, *Oceanology*, *15*, 719-721, 1975.

J. A. Goff, University of Texas Institute for Geophysics, 8701 N. MoPac Expressway, Austin, TX 78759. (e-mail: goff@utig.ig.utexas.edu)

B. E. Tucholke, Woods Hole Oceanographic Institution, Woods Hole, MA 02543. (e-mail: btucholke@whoi.edu)